research papers

CrossMark

Usage of CO_2 microbubbles as flow-tracing contrast media in X-ray dynamic imaging of blood flows

Sang Joon Lee,[a]* Han Wook Park[a] and Sung Yong Jung[b]

[a]Center for Biofluid and Biomimic Research, Department of Mechanical Engineering, Pohang University of Science and Technology (POSTECH), Pohang 790-784, Republic of Korea, and [b]Hyundai Heavy Industries, Ulsan 682-792, Republic of Korea. *E-mail: sjlee@postech.ac.kr

X-ray imaging techniques have been employed to visualize various biofluid flow phenomena in a non-destructive manner. X-ray particle image velocimetry (PIV) was developed to measure velocity fields of blood flows to obtain hemodynamic information. A time-resolved X-ray PIV technique that is capable of measuring the velocity fields of blood flows under real physiological conditions was recently developed. However, technical limitations still remained in the measurement of blood flows with high image contrast and sufficient biocapability. In this study, CO_2 microbubbles as flow-tracing contrast media for X-ray PIV measurements of biofluid flows was developed. Human serum albumin and CO_2 gas were mechanically agitated to fabricate CO_2 microbubbles. The optimal fabricating conditions of CO_2 microbubbles were found by comparing the size and amount of microbubbles fabricated under various operating conditions. The average size and quantity of CO_2 microbubbles were measured by using a synchrotron X-ray imaging technique with a high spatial resolution. The quantity and size of the fabricated microbubbles decrease with increasing speed and operation time of the mechanical agitation. The feasibility of CO_2 microbubbles as a flow-tracing contrast media was checked for a 40% hematocrit blood flow. Particle images of the blood flow were consecutively captured by the time-resolved X-ray PIV system to obtain velocity field information of the flow. The experimental results were compared with a theoretically amassed velocity profile. Results show that the CO_2 microbubbles can be used as effective flow-tracing contrast media in X-ray PIV experiments.

Keywords: CO_2 microbubbles; flow-tracing contrast media; biofluid flow; X-ray imaging; particle image velocimetry.

1. Introduction

Circulatory vascular diseases are one of the main causes of mortality. Abnormal blood flows with low wall shear stress were observed in regions affected by cardiovascular diseases (Hove et al., 2003). The quantitative velocity information of abnormal blood flows is important for the early diagnosis of cardiovascular diseases. Non-invasive imaging techniques are required to measure blood flows in vivo.

Among the various types of non-invasive imaging techniques, X-ray imaging techniques with high temporal and spatial resolutions are used to investigate hemodynamic characteristics. X-ray angiography provides only anatomical information on blood vessels and not quantitative flow information. The velocity fields of opaque biofluid flows were measured by adopting X-ray particle image velocimetry (PIV) (Lee & Kim, 2005a; Lee et al., 2009). This technique combines the merits of both X-ray imaging and PIV techniques. The X-ray PIV technique has been applied to observe blood flows in an opaque tube (Kim & Lee, 2006). However, these studies were conducted at low Reynolds numbers. A time-resolved X-ray PIV technique was developed to measure flows at a high Reynolds number (Jung et al., 2013). This technique was applied to observe blood flows under ex vivo conditions (Jamison et al., 2012).

Although the X-ray PIV technique has been gradually improved for a decade, some problems remain in its practical applications. One such problem is the deficiency of proper tracer particles suitable for X-ray PIV measurements. Although tracer particles such as silver-coated hollow glass beads (Im et al., 2007), alumina particles (Lee & Kim, 2003) and tungsten oxide particles (Lee et al., 2009) have been employed in X-ray PIV experiments, such particles are not bio-compatible. The speckle patterns of red blood cells (RBCs) were also used to measure the velocity information of blood flows in an X-ray PIV experiment (Kim & Lee, 2006). However, considering the blurring and noise caused by the surrounding tissues of blood vessels, this approach was diffi-

cult to apply in *in vivo* experiments. Although microparticles made of iopamidol encapsulated by polyvinyl alcohol were suitable in terms of biocompatibility (Lee *et al.*, 2010), the X-ray absorption coefficient of such microparticles was not enough for *in vivo* measurements. Gold nanoparticles (Au NPs) incorporated into chitosan were found to provide a high X-ray absorption rate (Jung *et al.*, 2012a). However, most Au NPs agglomerated in blood flows. Given the technological limitations of tracer particles, the development of a new particle for X-ray PIV experiments is necessary.

CO_2 gas has been widely used as an efficient X-ray contrast material in clinical angiographic imaging because of its high X-ray contrast (Durant *et al.*, 1957; Rautenberg, 1994). In the 1960s, CO_2 gas was used to obtain angiographic images of the inferior vena cava and portal vein (Hipona & Park, 1967). Compared with iodine contrast media, CO_2 gas did not exhibit hypersensitivity reactions (Song *et al.*, 1999). The intravascular supply of CO_2 gas did not significantly change the pH, pCO_2 and pO_2 levels. No significant histological change and no difference in renal blood flows were also observed compared with iodinated contrast agents (Kerns & Hawkins, 1995). Although the risks of CO_2 angiography exist (Kerns & Hawkins, 1995), the safe ranges of the injection rate and volume were already well known.

Hollow-type microparticles were reported to be suitable as flow tracers in X-ray PIV measurements (Lee *et al.*, 2009). The visibility of hollow-type microparticles was greatly enhanced in phase-contrast X-ray images. In the present study, CO_2 microbubbles were fabricated as flow-tracing contrast media to enhance the phase contrast further. Optimal fabricating conditions were found by comparing the size and number density of CO_2 microbubbles. The duration time of the CO_2 fabricated microbubbles were also compared. The developed CO_2 microbubbles were used to measure the velocity fields of 40% hematocrit blood flowing in an opaque tube. The present CO_2 microbubbles will be useful to investigate the hemodynamic characteristics of vascular diseases by the X-ray PIV system.

2. Materials and methods

2.1. Microbubble generation

Microbubbles were fabricated by mixing 5% human serum albumin (HSA) at 25 cc and CO_2 gas at 20 cc. Approximately 20% HSA was purchased from ChungShibJa Pharmacy Co. Ltd (South Korea). The media of human serum albumin (HSA) is DI water which contains sodium chloride, sodium hydroxide and acetyl-tryptophane. The 5% HSA was produced by diluting 20% HSA in a phosphate buffered saline solution. Serum albumin is a common globular protein and has been widely adopted as the encapsulating shell material of many ultrasound contrast agents (Stride & Saffari, 2003). Jeon *et al.* (2002) homogenized a gas-acqueous mixture by moving the plungers of two syringes connected by a threeway stopcock. However, the acquired quantity of microbubbles is too small to obtain velocity information using a PIV technique
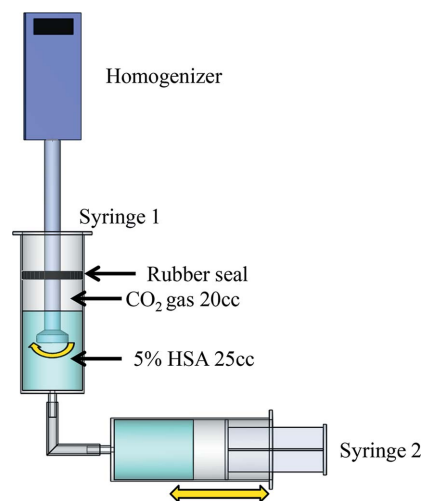

Figure 1
Schematic of the microbubble generator used in this study.

and the variation in microbubble size is large. Therefore, in this study, the technique is somewhat modified. Air bubbles have been known to produce arterial embolism. Significant embolic events, such as acute limb ischemia and cerebrovascular accident, are caused by air bubbles (Holcomb *et al.*, 2001). When venous air bubbles enter into the systemic arterial circulation, a paradoxical air embolism can be caused (Christin *et al.*, 2007). Although material properties are clearly distinguishable in X-ray images, it is difficult to differentiate CO_2 bubbles from air bubbles due to little difference in absorption and phase contrasts. The homogenizer is located in a CO_2 chamber to make it directly contact with CO_2 gas.

Fig. 1 shows a schematic of the microbubble generator used in the present study. Approximately 25 cc of 5% HSA and 20 cc of CO_2 gas were supplied into syringe 1. Syringe 1 was sealed with rubber to prevent the intake of outside air and leakage of the inside CO_2 gas. Syringe 2 was repeatedly pushed and pulled over ten times to mix the CO_2 gas and HSA. The sealing rubber positioned inside the syringe 1 was shifted following the movement of the syringe 2. Microbubbles were generated by mechanical agitation with a homogenizer (IKA-T25 digital ULTRA-TURRAX, IKA, Germany). The mixed solution was homogenized under various rotation speeds and agitating times. The rotation speed and agitation time varied from 3×10^3 r.p.m. to 15×10^3 r.p.m. and 1 min to 7 min, respectively. The optimal fabricating conditions were determined by comparing the visibilities of the X-ray images. Selected microbubbles were left in the 40% hematocrit blood until the number of particles per interrogation window was less than 15. Information on the generated microbubbles was acquired every 3 min.

2.2. X-ray imaging and image processing

A high-speed imaging system is required to minimize the displacement of microbubbles during the exposure time of the X-ray beam to measure the information on the fabricated
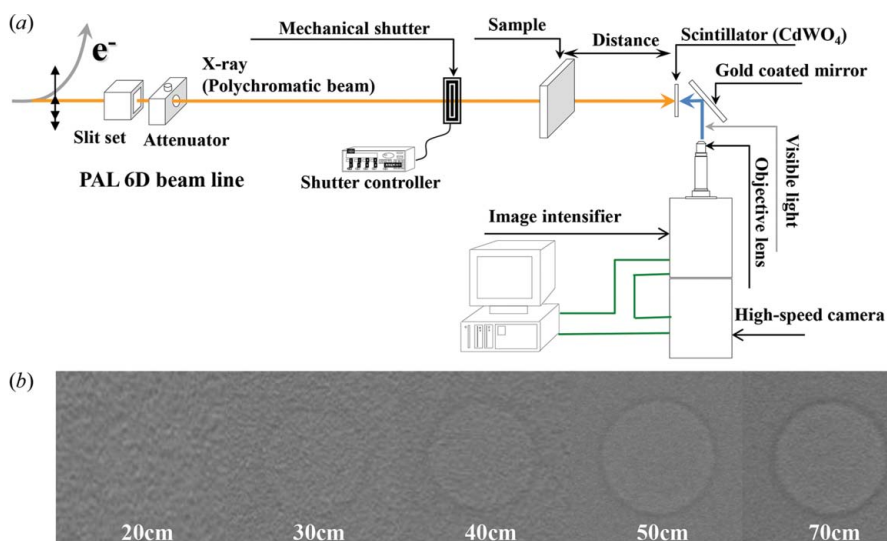
Figure 2
(*a*) Schematic of the time-resolved X-ray imaging system. (*b*) X-ray images of a microbubble at different distances between the sample and detectors.

microbubbles accurately. The number and average size of the fabricated microbubbles were measured by employing a time-resolved X-ray imaging system equipped with a high-speed camera. Fig. 2(*a*) shows a schematic of the X-ray imaging system. An image intensifier was attached in front of the camera. Experiments were conducted at the 6D beamline of the Pohang Light Source (PLS-II). The beam current was 202 mA and the storage energy of the synchrotron facility was 3 GeV. A polychromatic X-ray beam with beam flux of 2.2 × 10^{12} photon s^{-1} mm^{-2} was used in this experiment. The energy bandwidth and median energy of a 1 mm-thick silicon wafer are 18.6 and 23.54 keV, respectively. The beam size was 30 mm (H) × 5 mm (V). Several silicon wafers were installed in the pathway of the X-ray beam to minimize the damage by the strong X-ray beam flux on the biological samples. The test sample was placed approximately 30 m downstream from the source. Given that the biological samples provide a weak absorption contrast, the phase-contrast imaging technique was dominantly employed in this experiment. In phase-contrast X-ray imaging, the distance between the test sample and detector is important. Fig. 2(*b*) shows X-ray images of a microbubble according to the sample–detector distance. When the distance is too large, the captured images become blurred. The visibility of the microbubbles decreases with decreasing the distance. The optimal distance was 50 cm, at which sharp boundaries of the microbubbles were observed. All X-ray images were acquired at this distance.

As the X-ray beam passes through a CdWO$_4$ scintillator (500 μm thickness), X-rays are converted to visible light. The conversion efficiency of the scintillators depends on the type of scintillator. Therefore, the selection of a proper scintillator in compliance with the given experimental condition is important. X-ray images were recorded by using a high-speed camera (1024 pixels × 1024 pixels; Ultima-APX, Photron, Japan). The frame rate for X-ray PIV measurements was

2000 frames s^{-1}. It was reduced to 60 frames s^{-1} in the measurements of size and quantity of CO$_2$ microbubbles. The field of view was 1600 μm × 1600 μm with a 10× objective lens. The effective pixel size was 1.6 μm × 1.6 μm. An image intensifier (HiCATT; Lambert Instrument, The Netherlands) was attached in front of the camera to amplify the light intensity. Raw X-ray images contained noise caused by the amplification procedure. Each image had low contrast because of the short exposure time employed for high-speed imaging. The noise effect of the image intensifier decreased and the image contrast increased by adapting a flat-field correction, which has been widely employed in X-ray imaging experiments to improve image quality (Jung *et al.*, 2012*b*). Median and spatial frequency filters were also adopted to remove the noise effects (Jung *et al.*, 2013).

3. Result and discussion.

3.1. Size and number density of microbubbles

A typical X-ray image of CO$_2$ microbubbles is shown in Fig. 3(*a*). The scale bar indicates 50 μm. The image size is 200 μm (H) × 200 μm (V). In the X-ray image, the phase and absorption contrast effects simultaneously appear. The intensity difference caused by different absorption rates can be expressed by the Beer–Lambert law (Cullity & Stock, 2001),

$$I = I_0 \exp(-\mu x), \tag{1}$$

where I is the transmitted intensity and I_0 is the intensity of the incident X-ray beam. I and I_0 are obtained by averaging the intensities of the microbubbles and background, respectively. μ is the absorption coefficient of the test material. The transmitted intensity is influenced by penetration depth (x).
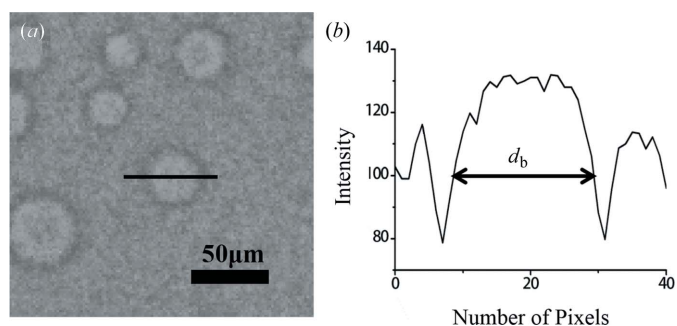

Figure 3
(*a*) Typical phase-contrast X-ray image of microbubbles. The scale bar indicates 50 μm. (*b*) Intensity variation along the solid line marked in (*a*). d_b represents the diameter of the microbubble in the image.

Therefore, I has different values with the variation of bubble size. Fig. 3(b) represents the intensity variation along the line marked in Fig. 3(a). The diameters of the microbubbles in the X-ray images were obtained by measuring the full width at half-maximum (FWHM) (Lee *et al.*, 2010). When the size of the microbubbles decreases and the amount of microbubbles increases, the ambiguity in the size measurement of the microbubbles in the X-ray images increases because of the overlapping microbubbles. Approximately 50 consecutive X-ray images were acquired at 60 frames s^{-1} to minimize such ambiguity. In the current study, the optimal amount of CO_2 microbubbles suitable for X-ray PIV measurements was evaluated in terms of microbubble diameter.

Fig. 4 shows variations in the average size and number of microbubbles in the 1000 μm depth. The analyzed image size is equal to the interrogation window of 64 pixels × 64 pixels in the PIV measurement. In the PIV experiments, the number of particles in each interrogation window should be greater than 15 (Keane & Adrian, 1990). Therefore, the total number of microbubbles in each interrogation window is adjusted to be greater than 15. The number and size of microbubbles at a fixed agitation time of 3 min are represented as bar and line graphs, respectively (Fig. 4a). The number of microbubbles rapidly increases with the increasing rotation speed of the homogenizer. The average value is 19.2, and the standard deviation is 1.30 at 15000 r.p.m. The size of the microbubbles gradually decreases with increasing rotation speed. The bubble size is 18.7 μm at 15000 r.p.m. Fig. 4(b) represents the variations in the number and diameter of microbubbles with
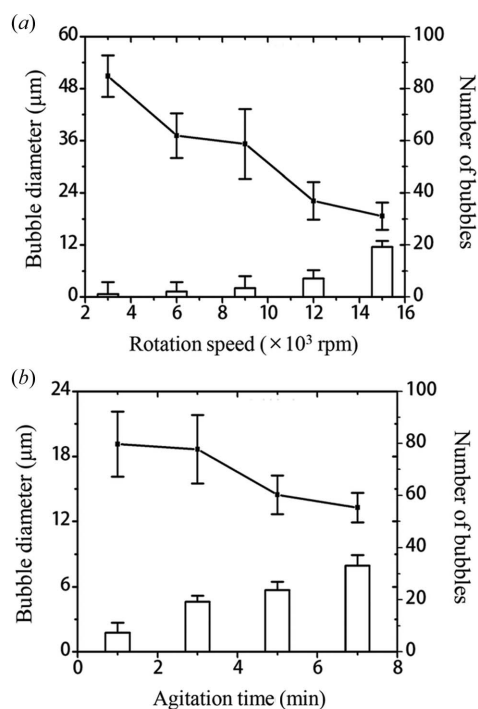
respect to the agitation time at a fixed rotation speed of 15000 r.p.m. The number of microbubbles continuously increases with increasing agitation time. The average number of microbubbles is 33.1 with a standard deviation of 4.05 at 7 min. The size of the microbubbles gradually decreases with increasing agitation times. The bubble size becomes 13.3 μm at 7 min. The spatial resolution of the time-resolved X-ray PIV system is approximately 5 μm at a frame rate of 2000 frames s^{-1}. However, microbubbles with diameters of less than 12 μm are not clearly defined under the tested flow condition. The rotation speed of 15000 r.p.m. at 7 min agitation is determined as the optimal condition for generating CO_2 microbubbles as tracer particles in X-ray PIV measurements. The total volume of generated microbubbles at the optimal condition in the chamber, 100 μm (H) × 100 μm (V) × 1000 μm (depth), is approximately 2.84×10^5 μm^3. The volume of RBCs in the same volume is approximately 4.0×10^6 μm^3. The volume fraction of microbubbles is 2.84% in the blood of 40% hematocrit. In the PIV experiment, the particle number density can affect the flow characteristics and accuracy. The number of microbubbles should be considered to minimize the interaction with RBCs. Therefore, the concentration of microbubbles needs to be adjusted with mixing plasma in each experimental condition.

The number and size of the residual microbubbles fabricated at the optimal condition were measured until the number of particles in an interrogation window became less than 15. An X-ray image was recorded every 3 min. The variations in the size and number of microbubbles during 19 min are 1.8 μm and 20.3, respectively (Fig. 5). The number of microbubbles is 14 at 16 min. Considering the measurement accuracy of PIV experiments, the consecutive recording of X-ray images was completed within 16 min. The number of microbubbles gradually decreases, but the size of the microbubbles slightly increases with time. Standard deviation in the measured bubble size also increases. CO_2 gas mixed with blood for 19 min. The injection volume was suggested in a previous parameter study (Kerns & Hawkins, 1995). CO_2 gas was supplied within the recommended volume rate to minimize the risk of embolism because of the mixing of CO_2 gas in the blood.

Figure 4
Variations of the average size and number of microbubbles (a) with varying rotation speed of the homogenizer at a fixed agitation time of 3 min and (b) with varying agitation time at a rotation speed of 15000 r.p.m.
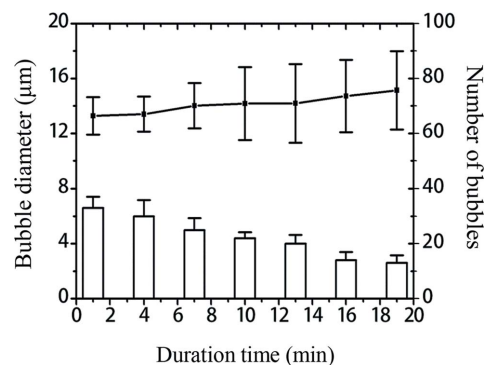

Figure 5
Variations in the size and number of residual microbubbles according to duration time. The rotation speed of the homogenizer and the agitation time are fixed at 15000 r.p.m. and 7 min, respectively.

Hollow CO_2 microbubbles have better image contrast as flow tracers compared with other tracer particles that have been used in X-ray PIV experiments. The diameter of a particle image can be estimated from the width of the auto-correlation peak (Adrian & Westerweel, 2011). In our preliminary experiments using the time-resolved X-ray PIV system with insufficient X-ray beam flux, the absorption contrast and phase-contrast effects of Sonazoid (GE Health-care, USA) used as an ultrasound contrast agent (UCA) were weakly observed. Thus, the particle-image diameter estimated from the width of the autocorrelation peak is different from the real diameter of the bubble. The width of the auto-correlation peak was estimated using the FWHM technique.

This difference may somewhat affect the measurement accuracy of PIV experiments. Given that most particles are less than 10 μm, the UCA Sonazoid is difficult to use as flow-tracing contrast media in X-ray PIV experiments. Silver-coated hollow particles have high image contrast, but are limited to non-clinical applications. It is difficult to observe individual Au NPs separately, due to the technological limitation in spatial resolution of the X-ray imaging system. Therefore, clusters of Au NPs have been used as flow-tracing contrast media. Considering that wall shear stress is estimated from the velocity gradient of the flow in the region near the vessel wall, Au NPs do not fit well for *in vivo* measurements of hemodynamic parameters.

Iopamidol was encapsulated by PVA as an absorption-based tracer particle. Therefore, the contrast of the X-ray image of the encapsulated particle was decreased under *in vivo* conditions because of the surrounding tissues and organs. This indicates that the signal-to-noise ratio (SNR) is not sufficient to conduct the X-ray PIV velocity field measurements with the PVA–iopamidol particles. In a previous study, Kariya *et al.* (2013) obtained images of abdominal aorta of a swine by using CO_2 microbubble as an absorption-based contrast agent. Therefore, its SNR was relatively low compared with other contrast agents. In this study, CO_2 microbubbles were used as phase-contrast-based tracer particles. In a biological sample, the phase-shift effect of an X-ray beam propagating through tissues is 1000 times larger than the loss of intensity caused by absorption contrast (Fitzgerald, 2001; Lewis, 2004). Therefore, CO_2 microbubbles which are employed as phase-contrast-based tracer particles are useful for investigating velocity information of opaque blood flows.

Although CO_2 microbubbles have several merits such as good biocompatibility, high image contrast and superior flow trackability, some problems still remain. The size and quantity of microbubbles are influenced by the surface tension of the mixture and the local pressure around the homogenizer. Therefore, generating microbubbles by following the guidelines suggested in this study is recommended.

3.2. Feasibility of microbubbles as flow-tracing contrast media

The velocity fields of 40% HCT blood flowing in a 1.5 mm-diameter opaque silicon tube were measured by using the time-resolved X-ray PIV system. Blood was supplied by a syringe pump at a flow rate of 1.9 ml min^{-1}. Microbubbles were seeded into the tube by using a syringe pump at a flow rate of 0.1 ml min^{-1}. The average flow rate in the tube was about 18.8 mm s^{-1}. The mixture of the microbubbles and blood was injected after fully stirring.

X-ray images were consecutively acquired at a frame rate of 2000 frames s^{-1} with an exposure time of 160 μs. Velocity information was obtained by applying a cross-correlation PIV algorithm to the X-ray images. The interrogation window was 64 pixels × 64 pixels with 50% overlapping. The mean velocity field was obtained by an ensemble averaging 500 instantaneous velocity fields statistically. The velocity vectors contain buoyancy effects caused by the density difference between the test blood and CO_2 gas. The terminal velocity of the microbubbles was determined by using a modified Stokes law (Lee & Kim, 2005b),

$$U_T = \frac{g d_b^2}{18\mu} \Delta\rho, \qquad (2)$$

where g is the gravitational acceleration and d_b is the diameter of the microbubbles. μ is the fluid viscosity and $\Delta\rho$ is the density difference. The terminal velocity of the microbubbles was calculated as 0.043 mm s^{-1}. The value of the terminal velocity was subtracted from PIV raw data. The maximum velocity measured at the centerline is approximately 22.08 mm s^{-1} at a Reynolds number of 11.75.

The X-ray images contain all velocity information obtained along the X-ray pathway. A mathematical formulation was adopted to compensate for the amassed volumetric flow information. The amassed velocity profile in a circular pipe can be represented as two-thirds of the velocity profile of the Poiseuille flow (Lee & Kim, 2003). Given that the blood flow has shear-thinning characteristics, the velocity profile of the blood flows in a circular pipe can be also be expressed as follows (Yeom *et al.*, 2014),

$$V(r) = V_{max}\left(1 - |r/R|^K\right), \qquad (3)$$

where K and R are the bluntness index and the radius of the circular tube, respectively. $V(r)$ represents the velocity at the radial position r, and V_{max} is the local maximum velocity at the center of the vessel. The K index was changed according to the flow and blood conditions.

Fig. 6(a) shows a schematic of the amassed flow velocity in a circular pipe. The whole velocity profiles along the X-ray propagation direction were integrated to obtain the amassed velocity profile with the relationship of $r^2 = x^2 + y^2$,

$$U_{Amassed}(x) = \frac{2 \int_0^{(R^2-x^2)^{1/2}} V_{max}\left(1 - |x/R|^K\right) dy}{2(R^2 - x^2)^{1/2}}$$
$$= \alpha(x) V_{max}\left(1 - |x/R|^K\right), \qquad (4)$$

where $\alpha(x)$ represents the ratio of amassed velocity to the original velocity at radial position X/R. The α value was
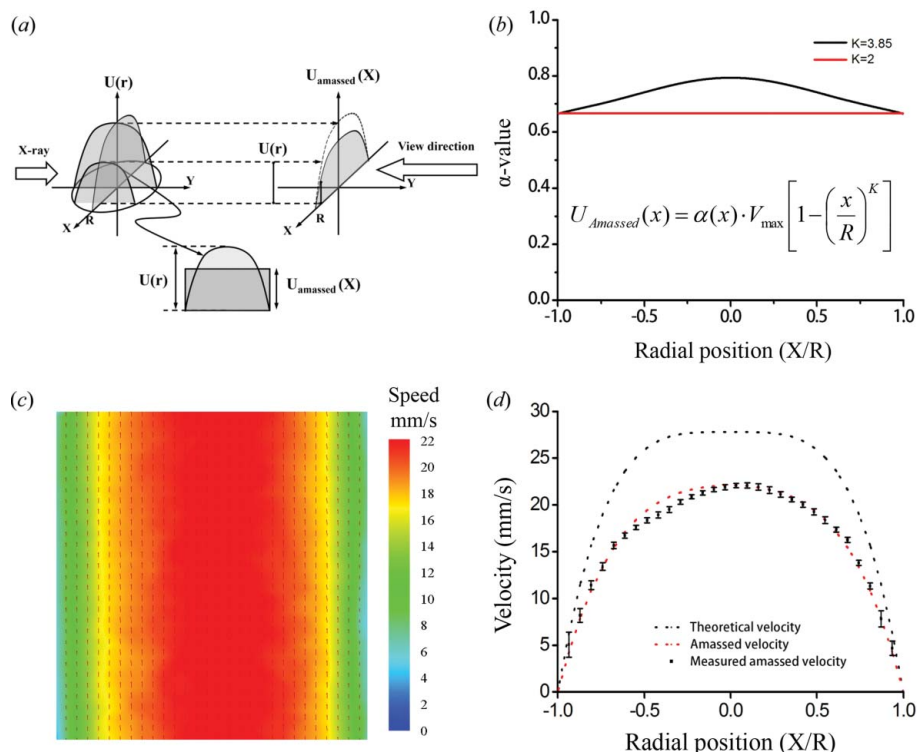
Figure 6
(a) Schematic of the amassed velocity profile. (b) Variations of the α value along the radial position for $K = 3.85$ and $K = 2$. (c) Mean velocity field of microbubbles seeded in blood flow of 40% hematocrit in a circular tube. (d) Comparison of streamwise mean velocity profiles: theoretical center-sectional velocity profile (black dots), theoretically amassed velocity profile (red dots) and measured amassed velocity profile (solid dots).

(2001) also revealed that the K index for a low Reynolds number blood flow measured with an intravital microscope was about 3.8. Therefore, the K index of 3.85 for the present study at a low Reynolds number blood flow seems to be reasonable. The reproducibility of the measured flow velocities was checked by statistical analysis of 18 velocity data sets. The mean velocity field of each data set was obtained by ensemble averaging of 100 instantaneous velocity fields. Fig. 7 shows variation of the centerline velocity for each data set at different flow rate. Error bars represent standard deviation of the centerline velocity. The measurement accuracy of PIV experiments is usually larger than 0.1 pixel for each displacement (Westerweel, 2000) and the theoretical corresponding error is ± 0.32 mm s^{-1} for the present experimental conditions. In these experiments, the standard deviation of the centerline maximum velocity was 0.396. The average flow rate was 1.978 ml min^{-1} and the standard deviation was 0.048. A red line indicates the injection flow rate of 2.0 ml min^{-1}. The difference between the measured and injected flow rates is approximately 1.1%. The microsphere method is reported to have around 5% in statistical flow estimation (Prinzen & Bassingthwaighte, 2000; Nose et al., 1985). PET has about 10% error (Su et al., 2013) and MRI velocimetry has at least 3% error (Kadbi et al., 2014). These results show that the measurement accuracy of the synchrotron X-ray PIV method is sufficient to measure blood flows.

In the present study, CO_2 microbubbles are demonstrated to be suitable as flow-tracing contrast media for X-ray PIV measurements of blood flows. The measured flow rate and velocity are well matched with those of theoretical prediction.
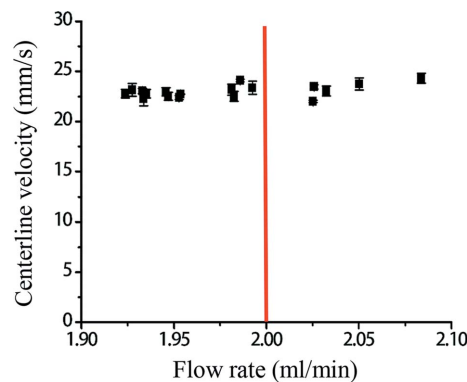
obtained by Romberg integration at each radial position. The radial position was uniformly divided into 6232 regions, and the circular pipe was divided into 3.049×10^7 segments. The theoretically amassed velocity profile and experimental results were curve-fitted iteratively with a varying K index. The ideal K index is 3.85. The maximum coefficient of determination in the fitted curves is 0.9945, and the difference in velocity data is 3.34%. Fig. 6(b) shows variations of the α value for $K = 2$ (Poiseuille flow) and $K = 3.85$ (shear-thinning flow). The α value for the Poiseuille flows is fixed at 2/3, whereas the α value at $K = 3.85$ appears as a function of radial position. The α values for $K = 3.85$ is curve-fitted into a sixth-order polynominal with $R^2 = 0.9999$. Fig. 6(c) represents the time-averaged velocity field of a blood flow without compensating for the buoyancy effects. Fig. 6(d) shows the streamwise mean velocity profiles of the blood flow. Solid dots denote the measured velocity data, including the buoyancy effect of microbubbles. The black dashed line represents the theoretical velocity profile, and the red dashed line indicates the amassed velocity profile at $K = 3.85$. The error bars represent the standard deviation of each velocity data. The standard deviation of each velocity component was about 0.3794. The error level increases with the increase of radial distance from the tube center. Tangelder et al. (1986) measured velocity profiles using a fluorescence microscopy. The bluntness index (K index) for the measured velocity profiles was varied from 2.4 to 4, depending on experimental conditions. Bishop et al.

Figure 7
Variation of the ensemble-averaged centerline velocity according to flow rate.

X-ray images of CO_2 microbubbles were acquired using the phase-contrast X-ray imaging technique. The phase-contrast X-ray imaging technique has been widely used in biomedical applications (Zhou & Brahme, 2008; Takeda *et al.*, 2002). Although the velocity field information of blood flows was obtained, the synchrotron facility availability and dose limitations still remained for clinical applications. These limitations will be overcome in the near future with technological advances in X-ray sources by which phase-contrast X-ray images can be acquired (Hemberg *et al.*, 2003; Tuohimaa *et al.*, 2007; Lundström *et al.*, 2012). Therefore, the CO_2 microbubbles method proposed in this study can be used to investigate blood flows of animal models in the present stage. However, the ultimate goal of this experimental technique is to investigate hemodynamic characteristics of cardiovascular diseases under *in vivo* clinical applications in the future.

4. Conclusion

Several tracer particles developed for X-ray PIV experiments have been tested to measure flows in an opaque conduit. However, tracer particles have technological limitations in practical applications to measure blood flows, due to toxicity and low image contrast. Hollow CO_2 microbubbles were fabricated in this study by mechanical agitation to overcome these technological limitations. They were fabricated at various operating conditions in terms of the rotation speed of the homogenizer and agitation time to determine the optimal fabrication condition. The optimal microbubbles were generated at a rotation speed of 15000 r.p.m. of the homogenizer at an agitation time of 7 min. The size of the microbubbles at the optimal condition is 13.3 μm, and the number of microbubbles is approximately 33.1. The feasibility and usefulness of the developed CO_2 microbubbles as flow-tracing contrast media were verified, and the velocity field of a blood flow in a circular tube was successfully measured within a 3.34% error level. Compared with other tracer particles, CO_2 microbubbles are convenient to use and easy to fabricate. They also have high image contrast and superior biocapability. These hollow CO_2 microbubbles will have strong potential in the X-ray PIV measurements of blood flows for investigating hemodynamic characteristics.

References

Adrian, R. J. & Westerweel, J. (2011). *Particle Image Velocimetry.* Cambridge University Press.

Bishop, J. J., Nance, P. R., Popel, A. S., Intraglietta, M. & Johnson, P. C. (2001). *Am. J. Physiol. Heart Circ. Physiol.* **208**, H222–H236.

Christin, F., Bouffard, Y., Rossi, R. & Delafosse, B. (2007). *Echocardiography*, **24**, 867–869.

Cullity, B. D. & Stock, S. R. (2001). *Elements of X-ray Diffraction.* New Jersey: Prentice Hall.

Durant, T. M., Stauffer, H. M., Oppenheimer, M. J. & Paul, R. E. (1957). *Ann. Int. Med.* **47**, 191–201.

Fitzgerald, R. (2001). *Phys. Today*, **54**(4), 21.

Hemberg, O., Otendal, M. & Hertz, H. M. (2003). *Appl. Phys. Lett.* **83**, 1483.

Hipona, F. A. & Park, W. M. (1967). *Am. J. Roentgenol. Radium Ther. Nucl. Med.* **99**, 606–611.

Holcomb, B. W., Loyd, J. E., Byrd, B. F., Wilsdorf, T. T., Casey-Cato, T., Mason, W. R. & Robbins, I. M. (2001). *Chest*, **119**, 1602–1605.

Hove, J. R., Köster, R. W., Forouhar, A. S., Acevedo-Bolton, G., Fraser, S. E. & Gharib, M. (2003). *Nature (London)*, **421**, 172–177.

Im, K. S., Fezzaa, K., Wang, Y. J., Liu, X., Wang, J. & Lai, M. C. (2007). *Appl. Phys. Lett.* **90**, 091919.

Jamison, R. A., Siu, K. K. W., Dubsky, S., Armitage, J. A. & Fouras, A. (2012). *J. Synchrotron Rad.* **19**, 1050–1055.

Jeon, D. S., Luo, H., Iwami, T., Miyamoto, T., Brasch, A. V., Mirocha, J., Naqvi, T. Z. & Siegel, R. J. (2002). *J. Am. Collect. Cardiol.* **39**, 124–129.

Jung, S. Y., Ahn, S., Nam, K. H., Lee, J. P. & Lee, S. J. (2012*a*). *Int. J. Cardiovas. Imaging*, **28**, 1853–1858.

Jung, S. Y., Lim, S. M. & Lee, S. J. (2012*b*). *J. Hydrol.* **452**, 83–89.

Jung, S. Y., Park, H. W., Kim, B. H. & Lee, S. J. (2013). *J. Synchrotron Rad.* **20**, 498–503.

Kadbi, M., Negahdar, M. J., Cha, J. W., Traughber, M., Martin, P., Stoddard, M. F. & Amini, A. A. (2014). *Magn. Reson. Med.* doi:10.1002/mrm.25188.

Kariya, S., Komemushi, A., Nakatani, M., Yoshida, R., Sawada, S. & Tanigawa, N. (2013). *Clin. Radiol.* **68**, 346–351.

Keane, R. D. & Adrian, R. J. (1990). *Meas. Sci. Technol.* **1**, 1202–1215.

Kerns, S. R. & Hawkins, I. F. Jr (1995). *Am. J. Roentgenol.* **164**, 735–741.

Kim, G. B. & Lee, S. J. (2006). *Exp. Fluids*, **41**, 195–200.

Lee, S. J., Jung, S. Y. & Ahn, S. (2010). *Biosens. Bioelectron.* **25**, 1571–1578.

Lee, S. J. & Kim, G. B. (2003). *J. Appl. Phys.* **94**, 3620.

Lee, S. J. & Kim, G. B. (2005*a*). *J. Appl. Phys.* **97**, 064701.

Lee, S. J., Kim, G. B., Yim, D. H. & Jung, S. Y. (2009). *Rev. Sci. Instrum.* **80**, 033706.

Lee, S. J. & Kim, S. (2005*b*). *Exp. Fluids*, **39**, 490–495.

Lewis, R. A. (2004). *Phys. Med. Biol.* **49**, 3573–3583.

Lundström, U., Larsson, D. H., Burvall, A., Takman, P. A. C., Scott, L., Brismar, H. & Hertz, H. M. (2012). *Phys. Med. Biol.* **57**, 2603–2617.

Nose, Y., Nakamura, T. & Nakamura, M. (1985). *Basic Res. Cardiol.* **80**, 417–429.

Prinzen, F. W. & Bassingthwaighte, J. B. (2000). *Cardiovasc. Res.* **45**, 13–21.

Rautenberg, E. (1994). *Deutsch. Med. Wochenschr.* **40**, 1205.

Song, K., Cho, D., Shinn, K., Charlton, E. & Cho, K. (1999). *Invest. Radiol.* **34**, 151–155.

Stride, E. & Saffari, N. (2003). *Proc. IME. H.* **217**, 429–447.

Su, Y., Arbelaez, A. M., Benzinger, T. L. S., Snyder, A. Z., Vlassenko, A. G., Mintun, M. A. & Raichle, M. E. (2013). *J. Cereb. Blood Flow Metab.* **33**, 115–121.

Takeda, T., Momose, A., Wu, J., Yu, Q., Zeniya, T., Thet-Thet-Lwin, Yoneyama, A. & Itai, Y. (2002). *Circulation*, **105**, 1708–1712.

Tangelder, G. J., Slaaf, D. W., Muijtjens, A. M. M., Arts, T., oude Egbrink, M. G. A. O. & Reneman, R. S. (1986). *Circ. Res.* **59**, 505–514.

Tuohimaa, T., Otendal, M. & Hertz, H. M. (2007). *Appl. Phys. Lett.* **91**, 074104.

Westerweel, J. (2000). *Exp. Fluids*, **29**, S3–S12.

Yeom, E., Nam, K. H., Paeng, D. G. & Lee, S. J. (2014). *Ultrasonics*, **54**, 205–216.

Zhou, S. A. & Brahme, A. (2008). *Phys. Med.* **24**, 129–148.